Molecular Dynamics Simulation Studies of the Structure of a Mixed Carbonate/LiPF6 Electrolyte near Graphite Surface as a Function of Electrode Potential

3 AUTHORS, INCLUDING:

Oleg Borodin
Army Research Laboratory

182 PUBLICATIONS **4,079** CITATIONS

Molecular Dynamics Simulation Studies of the Structure of a Mixed Carbonate/LiPF$_6$ Electrolyte near Graphite Surface as a Function of Electrode Potential

Jenel Vatamanu,*,[†] Oleg Borodin,[‡] and Grant D. Smith[†]

[†]Deparment of Material Science and Engineering, University of Utah, 122 South Central Campus Drive, Salt Lake City, Utah 84112, United States

[‡]Electrochemistry Branch, Army Research Laboratory, 2800 Powder Mill Road, Adelphi, Maryland 20783, United States

ABSTRACT: Molecular dynamics (MD) simulations of an electrolyte comprised of ethylene carbonate (EC), dimethyl carbonate (DMC), and LiPF$_6$ salt near the basal face of graphite electrodes have been performed as a function of electrode potential. Upon charging of the electrodes, the less polar DMC molecule is partially replaced in the interfacial electrolyte layer by the more polar EC. At negative potentials, the carbonyl groups from the carbonate molecules are repelled from the surface, while at positive potentials, we find a substantial enrichment of the surface with carbonyl groups. PF$_6^-$ rapidly accumulates at the positive electrode with increasing potential and vacates the negative electrode with increasing negative potential. In contrast, Li$^+$ concentration in the interfacial layer is found to be only weakly dependent on potential except at very large negative potentials. Hence, both composition of the electrolyte at the electrode surface and solvent environment around Li$^+$ are observed to vary dramatically with the applied potential with important implications for oxidation/reduction of the electrolyte and the process of Li$^+$ intercalation/deintercalation.
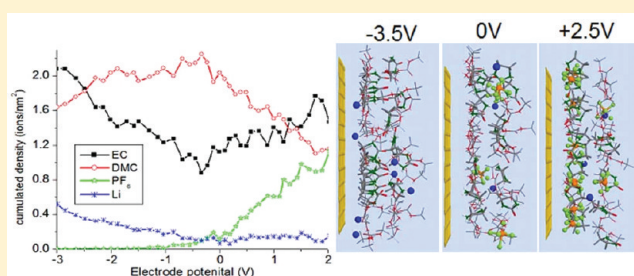
1. INTRODUCTION

The interface between the electrolyte and the electrodes is central to the operation of lithium ion batteries. Reduction of the electrolyte at the anode surface and oxidation at the cathode surface result in decomposition products that comprise the solid electrolyte interface (SEI) layers that ultimately passivate the electrodes and protect the electrolyte from further decomposition.[1] The structure of the SEI is believed to depend on the composition of the lithium solvation shell[2] highlighting the importance of its characterization next to interface. Furthermore, Li$^+$ must be transported through the electrode/electrolyte interface during charging/discharging processes giving rise to interfacial resistance that could exceed resistance of bulk electrolytes at low temperature.[3−5] It is clear that elucidating the properties of the interface between the electrolyte and the electrode is important to understanding the behavior of lithium ion batteries and ultimately to improving cycle life and minimizing the resistance to ion transport.
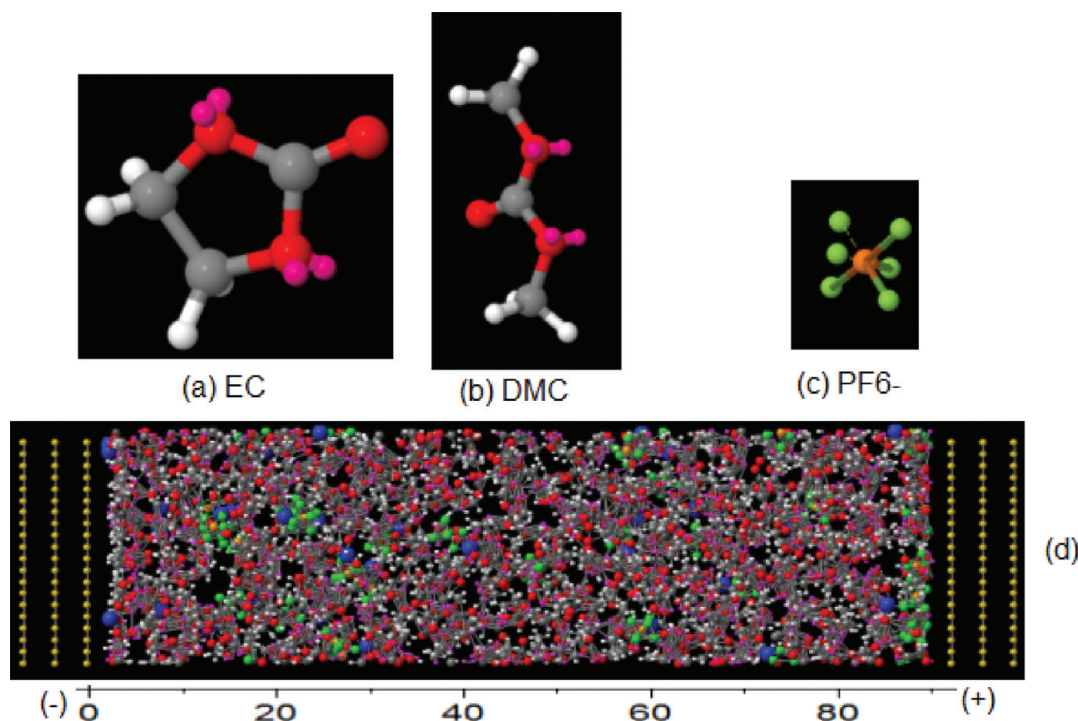
Mixed carbonate electrolytes, comprised of ethylene carbonate (EC, see Figure 1a) and one or more linear carbonates, such as dimethyl carbonate (DMC, see Figure 1b), doped with LiPF$_6$ (Figure 1c) represent the state of the art in electrolytes for commercial lithium ion batteries.[6] Classical[7−13] and ab initio[14] molecular dynamics (MD) simulation studies of ion transport and structure in carbonate electrolytes doped with LiPF$_6$ and other lithium salts as bulk electrolytes have been performed and have led to an improved understanding of Li$^+$ solvation and

transport mechanism. In contrast, simulations of mixed carbonate electrolytes at the interface with electrodes are quite limited.[15] These studies reveal that the composition of the electrolyte at the electrode surface and the manner in which Li$^+$ is solvated near the electrode surface can differ significantly from the bulk. This realization is important in understanding side reactions (reduction/oxidation) of the electrolyte, which depend upon the electrolyte solvent interaction with anion or Li$^+$ at the electrode interface,[16−18] as well as the processes of Li$^+$ intercalation and deintercalation, which involve desolvation/solvation of the Li$^+$ cation by the electrolyte at the electrode/electrolyte interface. Recently, the double-layer structure and differential capacitance of the ionic liquid−electrode interface has been extensively investigated in MD simulations.[19−24] However, these studies have not been extended to battery electrolytes that would include investigation of the influence of the electrode potential on the structure the lithium solvation shell, ion aggregation, ion surface enrichment, and capacitance. In this work, we extend our previous study of EC:DMC(3:7)/LiPF$_6$ electrolyte at the electrode surface[15] to include the influence of electrode potential for the mixed carbonate electrolyte double layer structure and capacitance and discuss implications of our findings to redox and lithium intercalation/deintercalation processes.

ACS Publications   © 2011 American Chemical Society

1114

dx.doi.org/10.1021/jp2101539 | *J. Phys. Chem. C* 2012, 116, 1114–1121

Figure 1. The chemical structure of (a) ethylene carbonate (EC), (b) dimethyl carbonate (DMC), and (c) PF_6^-. A snapshot of the 2D periodic simulation cell is shown in (d). The oxygen lone-pair on EC and DMC was modeled by placing off-atom centered charges shown in red in (a−b).

In this theoretical study, we investigated electrolyte behavior at potentials between electrodes up to 7 V, which is slightly higher than the redox stability window of EC:DMC/LiPF$_6$ electrolyte. The oxidative stability of EC and DMC-based electrolytes with BF$_4^-$ and PF$_6^-$ anions was measured[25] and was calculated using DFT methods[16] on glassy carbon to be around 6.2−6.7 V versus Li$^+$/Li, while the reduction potential[26,27] is around 1−1.4 V. Nevertheless, we think that it is valuable to obtain fundamental understanding of the double-layer behavior of electrolytes in simulations at the limit of their redox stability and slightly beyond it as this information cannot be easily obtained from experiments.

2. SIMULATION METHODOLOGY

An image snapshot of the simulation setup is shown in Figure 1d. The asymmetry direction of the system, that is, the direction perpendicular to the electrode surface, is our chosen z-axis. MD simulations were performed using a methodology that controls the potential difference between two electrodes[28,29] adapted for polarizable force fields. Charging of the electrode surface was computed under the assumption of a conductive surface maintained at the desired electrostatic potential and represented via flexible and Gaussian distributed (0.5 Å width) electrostatic charges on the atomic sites of the electrode.[30] In the context of our simulations, the assumed high conductor character of graphite employed here reflects a much faster distribution of electrostatic charges across the electrode than of the electrolyte ion diffusivity near the surface. More realistic models for graphite such as the tight-binding force field from ref 31 are expected to capture the semiconductor character of graphite.[32] Clearly, future work should explore this aspect, and a comparison with this work will be quite insightful in elucidating if the semiconductive character of the graphite is a critical factor determining

the electric double layer (EDL) structure and the shape of differential capacitance (DC).

The polarization of the electrolyte was represented via induced dipoles implemented through isotropic atomic polarizabilities. The short-range interactions between the induced dipoles were damped out utilizing the Thole method[33] with a Gaussian distribution. The electrode charges and the induced dipoles were computed iteratively subject to the condition of minimization of the electrostatic energy of the system with respect to the electrode fluctuant charges and the components of induced dipoles and subject to the constraint that the electrostatic potential on the electrode atoms is equal with the desired one. The (fixed) charges on electrolyte atoms were represented as point charges.

The equations of motion were integrated with a RESPA algorithm[34] over the following time resolutions: every 0.3 fs, the forces arising from the bond constrains (via Shake method), bond, angle, and out-of-plane vibrations were computed; every 1.5 fs, we updated the contributions of dihedral forces and nonbonded contributions within a range of 6.5 Å; and every 3 fs, a complete evaluation of the forces was performed. The induced dipoles were evaluated every 3 fs while the electrode charges were updated every 0.3 ps. The temperature was maintained constant using a Nose-Hoover thermostat[35] with a coupling time of 0.1 ps. Simulations were performed at 453 K. The short-range interactions were computed within a spherical cutoff of 10 Å, while the reciprocal part of Ewald summation was handled using a very efficient 2D-SMPE implementation described in ref 36 modified to include the contribution of the induced dipoles. All the bonds except those from PF$_6^-$ were constrained using the Shake method.[37] The electrolyte was modeled with polarizable version of APPLE&P force field[7] previously tested to reproduce well the bulk properties of

1115

dx.doi.org/10.1021/jp2101539 |*J. Phys. Chem. C* 2012, 116, 1114–1121

carbonate solvents and this electrolyte. The van der Waals interactions between the surface and the electrolyte atoms were determined using pairwise additive rules.[38]

Each electrode was represented by three layers of graphite having 240 carbon atoms and was oriented with the basal face toward the electrolyte as shown in Figure 1d. The cross section area of the electrode was 25.614×24.647 Å^2, and the distance between the electrodes (inner layers of carbon atoms) was 91.6 Å. This separation is sufficiently large to produce in the center of the simulation cell, along the z-direction, a region of about 15–20 Å width of bulklike electrolyte behavior. At 0 V applied potential, the electrolyte density in the center bulklike region of the simulation cell was the same as obtained in a 3-D periodic simulation of the same electrolyte at the same temperature and atmospheric pressure. The electrolyte consisted of 114 EC molecules, 256 DMC molecules, 31 PF$_6^-$ ions, and 31 Li$^+$ ions. Equilibration runs of at least 4 ns were performed; for systems of our size, this is sufficient time for the formation of EDL structure consistent with applied potential. After equilibration, we ran 27 production-run trajectories each at a different applied potential difference between electrodes ranging from 0 to 7 V of 25 ns length. Because of the increase in ion concentration near the electrode with increasing electrode potential (see below), the salt concentration in the bulk electrolyte (near the center of the simulation cell) decreases with increasing potential difference (by about 20% at 7 V relative to 0 V).

To estimate statistic errors associated with the presented density profiles and interfacial compositions of solvent and ions, we calculated the dispersion at each point of the density profile. Because closely spaced points along the trajectory are correlated, we grouped simulation data into consecutive blocks with increasing block size until consecutive blocks become uncorrelated following block average methodology described in Appendix D of Frenkel and Smit.[39] The block size of around 63 ps yielded uncorrelated measurements of the density profile resulting in 400 measurements. Interestingly, the Li-EC and Li-DMC residence times were found around 54 and 117 ps from bulk simulations indicating that solvent exchange also happens at the same time scale as the uncorrelated block size measurement. For most of the density profiles, the error bar is about 2% for PF$_6^-$, 3% for Li$^+$, 1.5% for EC, and 0.5% for DMC for a confidence interval of 80%. However, right at the interface, the error bars tend to increase up to a factor of 2–3. This increase of error bars in Helhmoltz layer is more pronounced for co-ions which anyway have a lower local density (as they are repealed from surface).

3. RESULTS AND DISCUSSION

As in our previous work, we define the electrode potential as the Poisson potential drop across the EDL relative to the potential of zero charge (RPZC)

$$U_{RPZC} = U_{EDL} - PZC = \varphi_{electrode} - \varphi_{bulk} - PZC \quad (1)$$

Here, U_{EDL} indicates the potential drop across the electrode/electrolyte interface and PZC is the potential of zero charge. The 1-D Poisson equation[40] was used to determine the electrostatic potential across the simulation cell

$$\nabla_z[\varepsilon_0(\nabla_z\varphi(z))] - \nabla_z\mu_z(z) = -\rho(z) \quad (2)$$

where ∇_z is the gradient in the z-direction, ε_0 is the vacuum permittivity, $\phi(z)$ is the Poisson potential, $\mu_z(z)$ is the density of the z-component of the induced dipoles, $\rho(z)$ is the charge
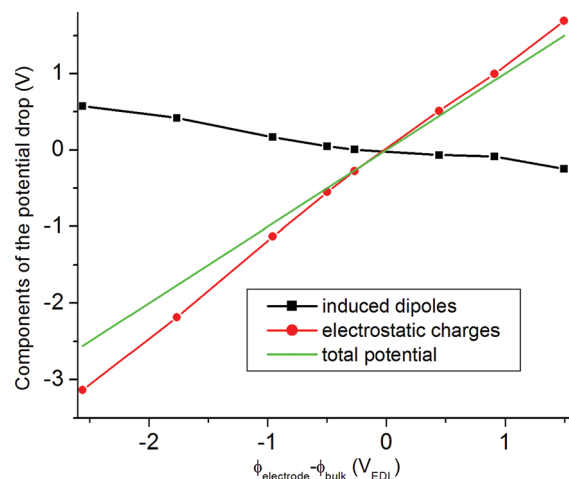
Figure 2. The electric double layer potential drop due to fixed charges and induced dipoles as a function of the potential drop across the electric double layer.

density, and z is the distance from the electrode surface. PZC was approximated from the Poisson potential drop across the EDL at an imposed potential difference between electrodes of $\Delta U = 0$ V. This approximation is reasonable because the total charge on the electrode at $\Delta U = 0$ V is negligibly small. For this system, PZC was -0.28 V. A negative PZC indicates relatively low densities of Li$^+$ ions near the uncharged surface, a large affinity of the uncharged surface for the negative oxygen atoms of carbonyl groups, and a small fraction of PF$_6^-$ adsorbed on the uncharged electrode surface (see below).

3.1. Role of Induced Dipoles on EDL Potential. Figure 2 shows the contribution of fixed partial atomic charges and induced atomic dipoles to the potential drop across the EDL as a function of U_{EDL}. As expected, the potential drop due to induced dipoles is opposite in sign to that of the fixed charge distribution (the induced dipoles in the EDL are in the direction of the electric field within the EDL and contribute an electric field in the opposite direction from that of the charged electrode). It is clear that inclusion of dipole polarizability has a large impact on the Poisson potential drop in the EDL especially at electrode potentials larger than 1 V in magnitude. Hence, the exclusion of dipole polarizability would result in a significantly different relationship between electrode charge and the electrode potential than observed for our polarizable model.
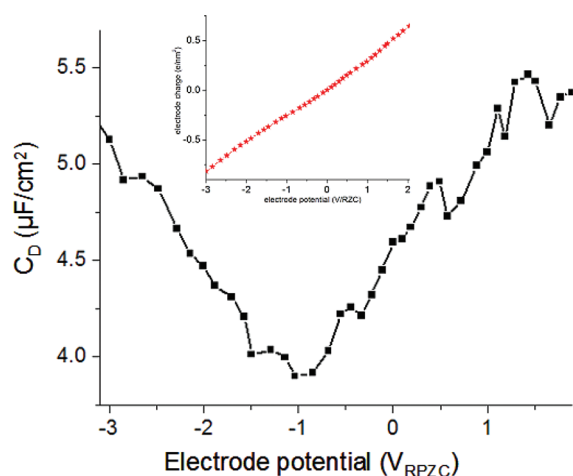
3.2. Differential Capacitance. The differential capacitance (DC) of an electrode is given as

$$DC = d\sigma/dU_{EDL} \quad (3)$$
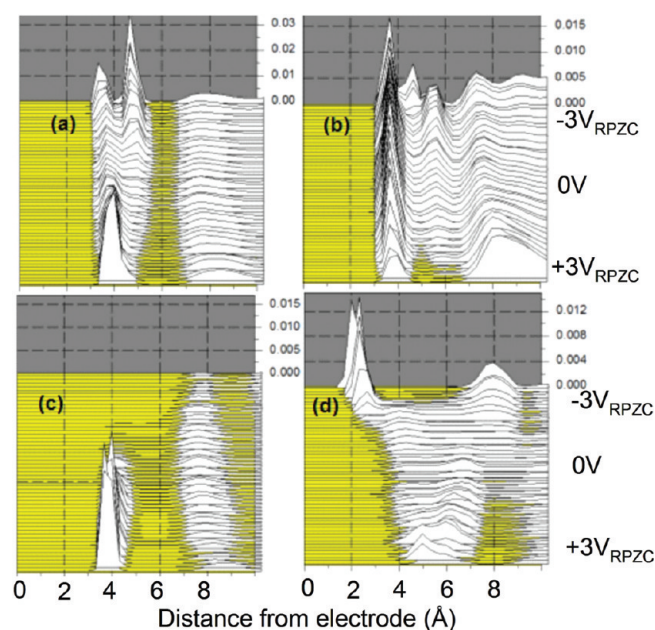
where σ is the electrode charge per unit surface area and U_{EDL} is the electrostatic potential drop across double layer (between the electrode and the bulk electrolyte). DC was computed by numerically differentiating the variation of the electrode charge as a function of the electrode potential, shown in the inset of Figure 3, as described in ref 41.

Figure 3 shows the resulting DC as a function of electrode potential. A U-shaped DC over a large potential range is observed. The U-shaped DC is expected according to Gouy–Chapman theory of dilute electrolyte solutions[42] because of sufficient empty space to accommodate additional ions at the electrode surface upon increasing electrode charge/potential. However, as discussed below, the ion density profiles do not

1116

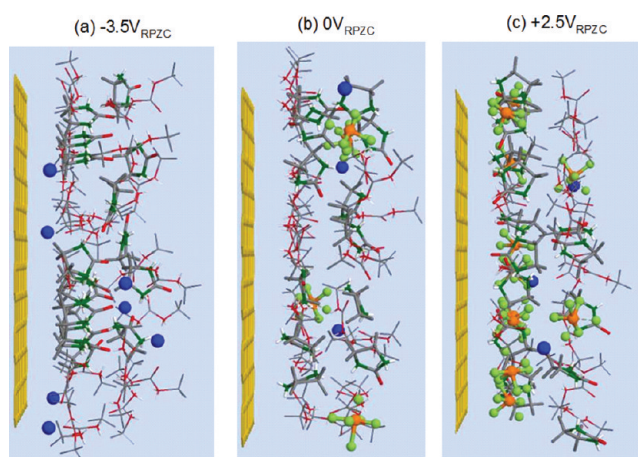dx.doi.org/10.1021/jp2101539 |*J. Phys. Chem. C* 2012, 116, 1114–1121

Figure 3. The differential capacitance as a function of the electrode potential. The corresponding electrode charge versus electrode potential is shown in the inset.


Figure 5. Image snapshots showing the electrolyte ordering near the interface at (a) large negative potential, (b) PZC, and (c) large positive electrode potential.

Figure 4. Molar mass density profiles as a function of the separation from electrode and applied potential for (a) EC, (b) DMC, (c) PF_6^-, and (d) Li^+. Represented on the x-axis is the distance between the two electrodes and on the y-axis is the electrode potential.

exhibit the structureless diffuse double layer behavior predicted by Gouy−Chapman theory. Finally, it is interesting to note that the minimum of DC is shifted significantly from PZC specifically at $U_{RPZC} = -1$ V. This shift is consistent with the very asymmetric behavior of the electrolyte structure at the negative and positive electrodes as described below.

3.3. Density Profiles. Figure 4 shows the density profiles of the electrolyte species as a function of distance from the electrode at various applied electrode potentials. These densities were calculated on the basis of the center-of-mass position of the molecules relative to the electrode surface. For all four electrolyte species, we observe a first layer within a distance of about 6 Å from the electrode surface and a second broader peak within a distance of 6−8 Å from the surface. Most of our discussion will be

focused on electrolyte structuring within 6 Å from the surface also shown in representative snapshots in Figure 5. For convenience, we refer to this first electrolyte layer as the surface layer.

As shown in Figure 4a and b, the density profiles EC and DMC within the surface layer at the negative electrode are split into two peaks with the first peak being within 4.5 Å and the second peak being 4.5−6 Å from the surface. For EC, parallel orientations of the five-member ring to the surface generate the inner peak, while perpendicular orientations of EC to surface (with C=O group pointing toward the surface or away from it) generate the EC density peak corresponding to the outer part of the surface layer. For DMC, the inner peak arises from DMC with its elongated axis (defined as the vector connecting the two ether oxygen atoms of DMC) parallel to the surface, and the outer peak arises from molecules with the same orientation further removed from the surface.

To quantify the extent of ion and solvent accumulation/removal from the surface layer as a function of electrode potential, we computed the number of molecules of each species within the first layer (i.e., within 6 Å from surface) per unit area (surface density) as a function of the applied potential as shown in Figure 6. At low potentials (close to 0 V_{RPZC}), the ratio [EC]/[DMC] near the electrode surface roughly matches the ratio in the bulk. As the potential increases (positively or negatively), the less polar DMC molecule is replaced by the more polar EC in the surface layer. For example, at −2.5 V and +1.2 V, [EC]/[DMC] in the surface layer becomes 1:1 compared to the bulk value of 1:2.24; above these potentials, the surface is richer in the minority EC than in DMC. Interestingly, the rate of DMC removal from the positive electrode with increasing potential is much lower than on the negative electrode while EC accumulation occurs somewhat more readily on the negative electrode. These effects can be associated with a rapid build up of PF_6^- on the positive electrode as discussed below.

Density profiles of Li^+ and PF_6^- ions (Figure 4 c, d and Figure 6) indicate dramatically different behavior of the two ions at the charged electrode surfaces. Specifically, PF_6^- exhibits a rapid increase in surface density with increasing positive potential and a rapid decrease in surface density with increasing negative potential. The density of Li^+ in the surface layer in contrast does not decrease on the positive plate with increasing positive

1117

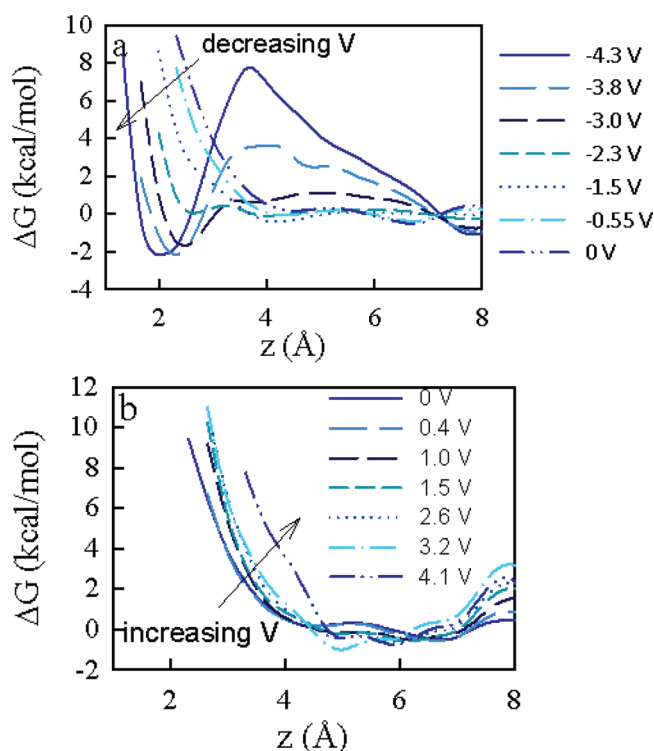dx.doi.org/10.1021/jp2101539 |J. Phys. Chem. C 2012, 116, 1114–1121
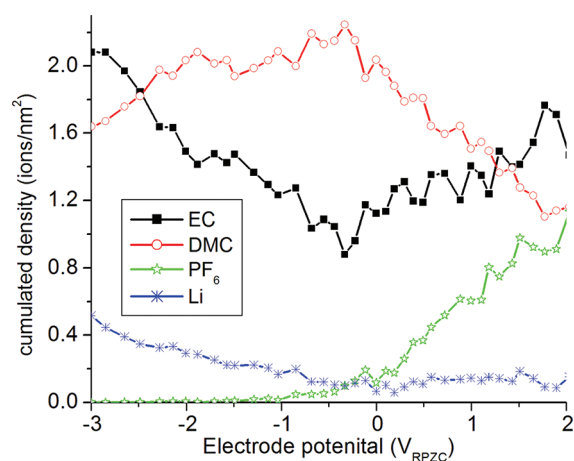
Figure 6. The cumulated density of electrolyte species in the interfacial layer, i.e., within 6.0 Å from the surface, as a function of the electrode potential.


Figure 7. The lithium potential of mean force (PMF) next to graphite electrode as a function of electrode potential. All potentials shown in the legends of this plot are the potentials drop within double layer relative to the potential of zero charge.

potential and shows a 2 times slower rate of increase with increasing negative potential compared to PF_6^- on the positive electrode. The larger DC shown in Figure 3 for a given positive electrode potential compared to the same negative electrode potential is consistent with the relative ease of accumulating PF_6^- on the positive electrode. However, the difference in DC between the positive and negative electrodes is not nearly as dramatic as the difference in the rate of accumulation/depletion of Li^+ and PF_6^- in the surface layer with changing potential indicating that (i) the fact that Li^+ can get closer to surface compensates in part for its lower accumulation rates than PF_6^- and (ii) the complex double layer structure both within the surface layer and beyond also influences the DC (e.g., see Figures 5 and 6).

For PF_6^-, we observe a sharp peak in density over a distance of 3−4.5 Å from the surface at positive potentials. At negative potentials, PF_6^- is almost completely removed from the surface layer. A second peak in PF_6^- density is observed in the range 6−9 Å from the electrode. The density peaks for Li^+ are clearly much broader than for PF_6^- except for electrode potentials more negative than −2 V, where we observe one single sharp density peak of Li^+ inserted between the first layer of solvent and the surface. Figure 4d illustrates the near complete absence of Li^+ in the inner part of the surface layer (<4.5 Å) except at large negative potentials. It can also be seen that a surprisingly high concentration of Li^+ is observed in the outer part of the surface layer even at large positive potentials. This behavior is consistent with that observed at LiFePO$_4$ interfaces[15] (for noncharged electrodes) and is due to the structuring of the solvent in the surface layer. Specifically, strongly structured solvent (with carbonyl oxygen atoms oriented largely toward or away from the surface) has a reduced ability to coordinate Li^+ cations within the inner part of the surface layer. Carbonyl oxygen atoms of carbonates oriented away from the interface can in contrast readily coordinate Li^+ in the outer part of the surface layer, where a broad Li^+ density peak is observed.

To better understand (partial) Li^+ desolvation from the electrolyte and adsorption onto the electrode surface, the potential of mean force ($\Delta G(z)$, i.e., the position dependent free energy) for the Li^+ cation as it crosses EDL was calculated as a function of distance from the graphite electrode using the

relationship

$$\Delta G(z) = - k_B T \log(\rho(z)) \tag{4}$$

where k_B is the Boltzmann constant, T is temperature, and $\rho(z)$ is the normalized (by the bulk Li^+ density) Li^+ density profile calculated perpendicular to graphite (z-direction). Figure 7a and b shows $\Delta G(z)$ for selected EDL potentials at the negative and positive electrolytes, respectively. At 0 V_{RPZC}, there is a very shallow minimum around 6−7 Å with $\Delta G(z)$ showing a sharp increase at distances below 4 Å indicating a significant free energy barrier that Li^+ needs to overcome in order to adsorb on the electrode surface. This increase in free energy as Li^+ approaches the uncharged electrode is due to partial loss of the solvation shell (partial desolvation) that may be exacerbated by structuring of the electrolyte (carbonates) at the surface. As the EDL potential decreases (larger negative potentials), the onset of the $\Delta G(z)$ increase monotonically shifts closer to the negative electrode from 4.0 Å at 0 V_{RPZC} to 2 Å at −4.3 V_{RPZC} corresponding to a lower free energy barrier for the Li^+ partial desolvation/surface adsorption. However, at the most negative EDL potentials, electrolyte structuring in the surface layer creates an additional barrier for Li^+ desolvation around 4 Å. This barrier increases as the potential becomes more negative. Examination of $\Delta G(z)$ on the positive electrode reveals a systematic, albeit small, shift of the upturn in $\Delta G(z)$ away from the electrode with increasing EDL potential. It indicates that the more positive the EDL voltage the higher the free-energy penalty to bring a cation to the surface as expected. We believe this is due in part to electrostatic interactions with the positively charged surface and in part to the highly structured nature of the electrolyte near the highly charged

1118

dx.doi.org/10.1021/jp2101539 |*J. Phys. Chem. C* 2012, 116, 1114−1121
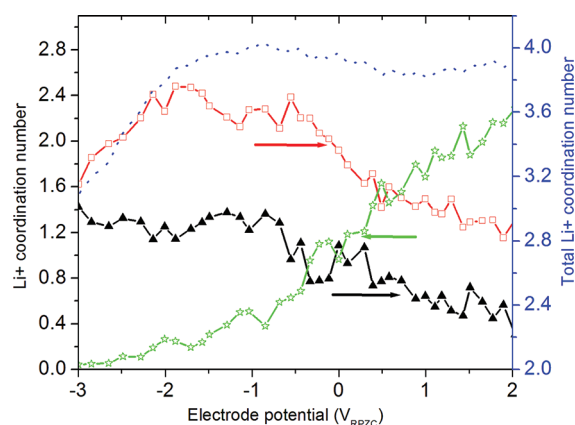
Figure 8. The coordination number around interfacial-layer Li^+ with the electrode potential for DMC (red line with open-square symbols), EC (black lines with filled triangles), and PF_6 (green line with start symbols). The total coordination number around Li^+ is represented by the dotted blue line.

Figure 9. The percentages of solvent located in our Helmholtz layer, coordinated with Li^+, as a function of the electrode potential.

surface. These results also indicate that the barrier/activation energy for the Li^+ desolvation for the higher voltage cathodes is expected to be higher than for lower voltage materials potentially limiting low-temperature operation of the former because of high interfacial impedance.

3.4. Li^+ Coordination. We observe that Li^+ in the bulk electrolyte is coordinated primarily with carbonyl groups and forms ion pairs and aggregates with PF_6^-. Only 10−15% of Li^+ do not have a counterion in their first solvation shell. We determined a coordination number for PF_6^-, carbonyl oxygen from EC, and carbonyl oxygen from DMC around each Li^+ by counting the number of each of these coordinating species with the first coordination shell as given by the minimum in the corresponding pair distribution function following the first peak, that is, within 2.8 Å from the Li^+ for oxygen atoms and within 4.4 Å for phosphorus atoms. Bulk Li^+ is coordinated with 1.1 ions of PF_6^- (as given by phosphorus coordination), 0.65 carbonyl oxygen atoms from EC, and 1.94 carbonyl oxygen atoms from DMC yielding a total coordination number around 3.7. The ratio of EC to DMC in the coordination shell of bulk Li^+ is quite similar to that observed at lower temperature and is dominated by the majority DMC which interacts favorably with the LiPF$_6$ ion pairs.[7]

Next, we analyzed the coordination number of Li^+ located in the surface layer as a function of the applied electrode potential. As shown in Figure 8, at low potentials (near PZC), the coordination of surface Li^+ is very similar to that of bulk Li^+. Upon charging the surface, the local environment around the surface Li^+ changes significantly. For example, at +2 V_{RPZC}, the interfacial Li^+ coordinates with around 0.4 EC, 1.3 DMC, and 2.2 PF_6^-. The increased role of PF_6^- in Li^+ coordination is expected at the positive electrode because of its high concentration in the surface layer. At the highly charged negative electrode (−2 V_{RPZC}), average Li^+ coordination involves 1.1 EC, 2.3 DMC, and 0.2 PF_6^-. The decreased importance of the anion and the increased importance of EC are qualitatively consistent with composition of the interfacial electrolyte layer. Quantitatively (on the basis of composition), we would expect even greater participation of EC in coordination Li^+ near the highly charged negative electrode. Detailed analysis of Li^+ solvation as a function of position within the layer reveals that Li^+ within the inner part of the surface layer
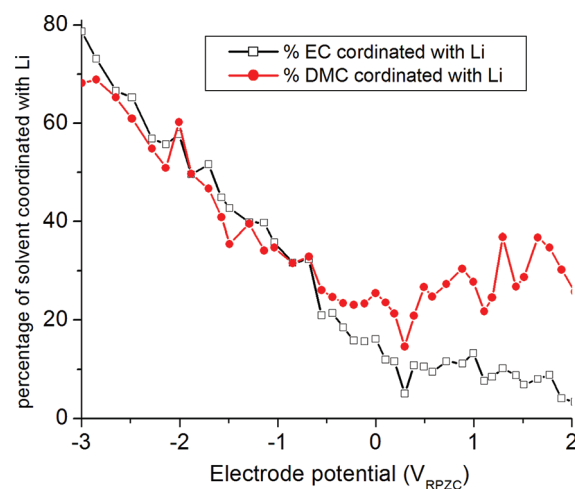
at high negative potentials is preferentially solvated by DMC despite the absence of PF_6^-. This is likely due to the stronger ordering of EC (with carbonyl oxygen pointing away from the negative surface) compared to DMC within the interfacial layer at high negative potentials because of higher dipole−surface interaction of EC. The total coordination of first-layer Li^+ with electrolyte is remarkably constant in the potential range −2 V_{RPZC} to +2 V_{RPZC}, and it is quite similar to bulk coordination. In the range −2 V_{RPZC} to −3 V_{RPZC}, however, the total coordination of Li^+ is around 3. The insertion of Li^+ near the surface at high negative potentials shown in Figure 5a has the net effect of replacing some Li^+−electrolyte coordination with Li^+−surface coordination.

Finally, we show in Figure 9 the percentage of EC and DMC in the surface layer that participates in coordination of Li^+. The affinity of the solvent in the first layer toward Li^+ is strongly influenced by the electrode potential. First, increasing negative potential increases Li^+ concentration in the surface layer thereby involving more EC and DMC in Li^+ coordination. Interestingly, at the positive electrode, the DMC is more involved with Li^+ than EC because the carbonyls of EC more strongly adsorb to the surface rather then being available to coordinate with Li^+. Hence, the Li^+ retention near the positive electrode observed in Figure 4 is achieved largely by strong bonding with the carbonyl groups of DMC.

4. CONCLUSIONS

This study demonstrates that the composition of the interfacial layer of electrolyte near graphite electrodes depends strongly on the electrode potential. For both positively and negatively charged electrodes, the amount of EC relative to DMC increases within increasing electrode charge. This observation is consistent with the observed dominance of EC decomposition compounds in SEI layers formed in many mixed electrolytes even when EC is the minority solvent component.[43] At the positive electrode, the density of PF_6^- increases rapidly with increasing electrode potential. This observation has important ramifications in understanding oxidation reactions where we have recently illustrated that the oxidative stability of solvent components is strongly influenced (reduced) by the presence of anions.[16,17] Finally, the low fraction of carbonates in the surface

1119

dx.doi.org/10.1021/jp2101539 | J. Phys. Chem. C 2012, 116, 1114–1121

layer involved with Li^+ coordination except at quite high negative potentials (Figure 9) has possible implications on solvent reduction. Specifically, the inner SEI layer in EC containing electrolytes on graphite is believed to be formed from doubly reduced EC which leads to the formation of Li_2CO_3 and $(CH_2OCO_2Li)_2$.[44] The propensity to form Li_2CO_3 versus $(LiCO_3CH_2)_2$ was observed to depend upon the amount of EC in a mixed EC/THF because of competition between the reactions $LiCO_3^- + Li^+ \rightarrow Li_2CO_3$ (preferred at low EC concentrations) and $LiCO_3^- + EC \rightarrow (CH_2OCO_2Li)_2 + C_2H_4$ (preferred at high EC concentrations). We speculate that the relative propensity for these reactions will also depend upon Li^+ near the interface with low Li^+ concentration favoring formation of $(CH_2OCO_2Li)_2$ over Li_2CO_3. Finally, the low probability of finding Li^+ within the interfacial layer except at very high negative potentials because of structuring of the solvent results in increased barriers to bringing Li^+ to the electrode surface and is likely a source of interfacial impedance.

■ AUTHOR INFORMATION

Corresponding Author
*E-mail: jenel.vatamanu@utah.edu.

■ ACKNOWLEDGMENT

■ REFERENCES

(1) (a) Xu, K.; von Cresce, A. J. Mater. Chem. **2011**, 21, 9849–9864. (b) Liu, J.; Manthiram, A. J. Electrochem. Soc. **2009**, 156, A66–A72. (c) Liu, J.; Manthiram, A. J. Phys. Chem. C **2009**, 113, 15073–15079. (d) Guo, J.; Chen, X.; Wang, C. J. Mater. Chem. **2010**, 20, 5035–5040. (e) Guo, J.; Wang, C. Chem. Commun. **2010**, 46, 1428–1430. (f) Koltypin, M.; Aurbach, D.; Nazar, L.; Ellis, B. J. Power Sources **2007**, 174, 1241–1250. (g) Song, S.; Baek, S. Electrochim. Acta **2009**, 54, 1312–1318. (h) Yamada, Y.; Iriyama, Y.; Abe, T.; Ogumi, Z. Langmuir **2009**, 25, 12766–12770. (i) Xu, M.; Zhou, L.; Chalasani, D.; Dalavi, S.; Lucht, B. L. J. Electrochem. Soc. **2011**, 158, A1202–A1206.

(2) (a) von Cresce, A.; Xu, K. Electrochem. Solid-State Lett. **2011**, 14, A154–A156. (b) Xu, K.; von Cresce, A.; Lee, U. Langmuir **2010**, 26, 11538–11543. (c) Jung, Y. S.; Cavanagh, A. S.; Riley, L. A.; Kang, S. H.; Dillon, A. C.; Groner, M. D.; George, S. M.; Lee, S. H. Adv. Mater. **2010**, 22, 2172–2176. (d) Mancini, M.; Nobili, F.; Dsoke, S.; D'Amico, F.; Tossici, R.; Croce, F.; Marassi, R. J. Power Sources **2009**, 190, 141–148. (e) Choi, N.; Yew, K.; Lee, K.; Sung, M.; Kim, H.; Kim, S. J. Power Sources **2006**, 161, 1254–1259. (f) Choi, N.; Yew, K.; Kim, H.; Kim, S.; Choi, W. J. Power Sources **2007**, 172, 404–409.

(3) Jow, T. R.; Allen, J.; Marx, M.; Nechev, K.; Deveney, B.; Rickman, S. ECS Trans. **2009**, 25, 3–12.

(4) Jow, T. R.; Zhang, S. S.; Xu, K.; Allen, J. L. ECS Trans. **2006**, 3, 51–58.

(5) (a) Ogumi, Z. Electrochemistry **2010**, 78, 319–324. (b) Nguyen, C. C.; Song, S.-W. Electrochim. Acta **2010**, 55, 3026–3033. (c) Hanai, K.; Ueno, M.; Imanishi, N.; Hirano, A.; Yamamoto, O.; Takeda, Y. J. Power Sources **2011**, 196, 6756–6761. (d) McCloskey, B. D.; Bethune, D. S.; Shelby, R. M.; Girishkumar, G.; Luntz, A. C. J. Phys. Chem. Lett. **2011**, 2, 1161–1166. (e) Das, S.; Bhattacharyya, A. J. J. Phys. Chem. B **2011**, 115, 2148–2154. (f) Smith, A. J.; Burns, J. C.; Xiong, D.; Dahn, J. R. J. Electrochem. Soc. **2011**, 158, A1136–A1142.

(6) (a) Xu, K. Chem. Rev. **2004**, 104, 4303–4418. (b) Lee, K.-H.; Song, S.-W. ACS Appl. Mater. Interfaces **2011**, 3, 3697–3703. (c) Wang, J.; Manga, K. K.; Bao, O; Loh, K. P. J. Am. Chem. Soc. **2011**, 133, 8888–8891. (d) Zhu, T.; Chen, J. S.; Lou, X. W. J. Phys. Chem. C **2011**, 115, 9814–9820.

(7) Borodin, O.; Smith, G. D. J. Phys. Chem. B **2009**, 113, 1763–1776.

(8) Borodin, O.; Smith, G. D. J. Phys. Chem. B **2006**, 110, 6279–6292.

(9) Borodin, O.; Smith, G. D. J. Phys. Chem. B **2006**, 110, 4971–4977.

(10) Borodin, O.; Smith, G. D. J. Phys. Chem. B **2006**, 110, 6293–6299.

(11) Borodin, O.; Smith, G. D. J. Solution Chem. **2007**, 36, 803–813.

(12) Wang, Y. X.; Balbuena, P. B. J. Phys. Chem. B **2004**, 108, 15694–15702.

(13) Takeuchi, M.; Kameda, Y.; Umebayashi, Y.; Ogawa, S.; Sonoda, T.; Ishiguro, S. I.; Fujita, M.; Sano, M. J. Mol. Liq. **2009**, 148, 99–108.

(14) (a) Ganesh, P.; Jiang, D.-e.; Kent, P. R. C. J. Phys. Chem. B **2011**, 115, 3085–3090. (b) Xing, L.; Li, W.; Xu, M.; Li, T.; Zhou, L. J. Power Sources **2011**, 196, 7044–7047.

(15) Smith, G. D.; Borodin, O.; Russo, S. P.; Rees, R. J.; Hollenkamp, A. F. Phys. Chem. Chem. Phys. **2009**, 11, 9884–9897.

(16) Borodin, O.; Jow, T. R. ECS Trans. **2011**, 33, 77–84.

(17) (a) Xing, L.; Borodin, O.; Smith, G. D.; Li, W. J. Phys. Chem. A **2011**, 115, 13896–13905. (b) Xing, L. D.; Wang, C. Y.; Xu, M. Q.; Li, W. S.; Cai, Z. P. J. Power Sources **2009**, 189, 689–692.

(18) (a) Yu, J.; Balbuena, P. B.; Budzien, J.; Leung, K. J. Electrochem. Soc. **2011**, 158, A400–A410. (b) Xing, L.; Wang, C.; Li, W.; Xu, M.; Meng, X.; Zhao, S. J. Phys. Chem. B **2009**, 113, 5181–5187. (c) Xing, L.; Li, W.; Wang, C.; Gu, F.; Xu, M.; Tan, C.; Yi, J. J. Phys. Chem. B **2009**, 113, 16596–16602.

(19) Vatamanu, J.; Borodin, O.; Smith, G. D. J. Phys. Chem. B **2011**, 115, 3073–3084.

(20) Vatamanu, J.; Cao, L.; Borodin, O.; Bedrov, D.; Smith, G. D. J. Phys. Chem. Lett. **2011**, 2, 2267–2272.

(21) Vatamanu, J.; Borodin, O.; Smith, G. D. J. Am. Chem. Soc. **2010**, 132, 14825–14833.

(22) Borodin, O.; Vatamanu, J.; Smith, G. D. ECS Trans. **2010**, 33, 583–599.

(23) Fedorov, M. V.; Kornyshev, A. A. J. Phys. Chem. B **2008**, 112, 11868–11872.

(24) Georgi, N.; Kornyshev, A. A.; Fedorov, M. V. J. Electroanal. Chem. **2010**, 649, 261–267.

(25) Ue, M.; Takeda, M.; Takehara, M.; Mori, S. J. Electrochem. Soc. **1997**, 144, 2684–2691.

(26) Vollmer, J. M.; Curtiss, L. A.; Vissers, D. R.; Amine, K. J. Electrochem. Soc. **2004**, 151 (1), A178–A183.

(27) Zhang, X. R.; Kostecki, R.; Richardson, T. J.; Pugh, J. K.; Ross, P. N. J. Electrochem. Soc. **2001**, 148, A1341–A1345.

(28) Reed, S. K.; Lanning, O. J.; Madden, P. A. J. Chem. Phys. **2007**, 126, 084704.

(29) Vatamanu, J.; Borodin, O.; Smith, G. D. Phys. Chem. Chem. Phys. **2010**, 12, 170–182.

(30) Siepmann, J. I.; Sprik, M. J. Chem. Phys. **1995**, 102, 511.

(31) Pastewka, L.; Javri, T. I.; Mayrhofer, L.; Moseler, M. Phys. Rev. B **2011**, 83, 165418–165424.

(32) (a) Gericher, H. J. Phys. Chem. **1985**, 89, 4249–4251. (b) Randin, J. P.; Yeager, E. Electroanal. Chem. **1972**, 36, 257–276.

(33) Thole, B. T. Chem. Phys. **1981**, 59, 341–350.

(34) Tuckerman, X. M. E.; Berne, B. J.; Martyna., G. J. J. Chem. Phys. **1990**, 97, 1990.

(35) Hoover, W. G. Phys. Rev. A **1985**, 31, 1695–1697.

(36) (a) Kawata, M.; Mikami, M. Chem. Phys. Lett. **2001**, 340, 157–164. (b) Kawata, M.; Nagashima, U. Chem. Phys. Lett. **2001**,

340, 165–172. (c) Kawata, M.; Mikami, M.; Nagashima, U. *J. Chem. Phys.* **2002**, *116*, 3430. (d) Kawata, M.; Mikami, M.; Nagashima, U. *J. Chem. Phys.* **2002**, *117*, 3526. (d) Kawata, M.; Mikami, M.; Nagashima, U. *J. Chem. Phys.* **2001**, *115*, 4457.

(37) Forester, T. R.; Smith, W. *J. Comput. Chem.* **1998**, *19*, 102–111.

(38) Borodin, O. *J. Phys. Chem. B* **2009**, *113*, 11463–11478.

(39) Frenkel, D.; Smit, B. *Understanding Molecular Simulations: From Algorithms to Applications*; Academic Press: San Diego, CA, 2002.

(40) Frydel, D. *J. Chem. Phys.* **2011**, *134*, 234704.

(41) Lamperski, S.; Outhwaite, C. W.; Bhuiyan, L. B. *J. Phys. Chem. B* **2009**, *113*, 6569.

(42) Grahame, D. C. *Chem. Rev.* **1947**, *41*, 441–501.

(43) (a) Bockris, J. O'M.; Reddy, A. K. N. *Modern Electrochemistry*, 2nd ed.; Plenum Press: New York, 2000; Vol. 2. (b) Fong, R.; von Sacken, U.; Dahn, J. R. *J. Electrochem. Soc.* **1990**, *137*, 2009–2013. (c) Dey, A. N.; Sullivan, B. P. *J. Electrochem. Soc.* **1970**, *117*, 222–224. (d) Aurbach, D.; Daroux, M. L.; Faguy, P. W.; Yeager, E. *J. Electrochem. Soc.* **1987**, *134*, 1611–1620. (e) Zhuang, G. V.; Yang, H.; Ross, P. N.; Xu, K.; Jow, T. R., Jr. *Electrochem. Solid-State Lett.* **2006**, *9*, A64–A68. (f) Zhuang, G. V.; Xu, K.; Yang, H.; Jow, T. R.; Ross, P. N., Jr. *J. Phys. Chem. B* **2005**, *109*, 17567–17573.

(44) Aurbach, D.; Levi, M. D.; Levi, E.; Schechter, A. *J. Phys. Chem. B* **1997**, *101*, 2195–2206.